Title
Investigation of CO2 Plume Behavior for a Large-Scale Pilot Test of Geologic Carbon Storage in a Saline Formation

Journal
Transport in Porous Media, 82(1)

ISSN
1573-1634

Author
Doughty, Christine

Publication Date
2010-03-01

DOI
10.1007/s11242-009-9396-z

Peer reviewed

Transp Porous Med (2010) 82:49–76
DOI 10.1007/s11242-009-9396-z

Investigation of CO_2 Plume Behavior for a Large-Scale Pilot Test of Geologic Carbon Storage in a Saline Formation

Christine Doughty

Received: 15 December 2008 / Accepted: 9 April 2009 / Published online: 9 May 2009

Abstract The hydrodynamic behavior of carbon dioxide (CO_2) injected into a deep saline formation is investigated, focusing on trapping mechanisms that lead to CO_2 plume stabilization. A numerical model of the subsurface at a proposed power plant with CO_2 capture is developed to simulate a planned pilot test, in which 1,000,000 metric tons of CO_2 is injected over a 4-year period, and the subsequent evolution of the CO_2 plume for hundreds of years. Key measures are plume migration distance and the time evolution of the partitioning of CO_2 between dissolved, immobile free-phase, and mobile free-phase forms. Model results indicate that the injected CO_2 plume is effectively immobilized at 25 years. At that time, 38% of the CO_2 is in dissolved form, 59% is immobile free phase, and 3% is mobile free phase. The plume footprint is roughly elliptical, and extends much farther up-dip of the injection well than down-dip. The pressure increase extends far beyond the plume footprint, but the pressure response decreases rapidly with distance from the injection well, and decays rapidly in time once injection ceases. Sensitivity studies that were carried out to investigate the effect of poorly constrained model parameters permeability, permeability anisotropy, and residual CO_2 saturation indicate that small changes in properties can have a large impact on plume evolution, causing significant trade-offs between different trapping mechanisms.

Keywords Geologic carbon storage · CO_2 sequestration · Multiphase flow modeling · CO_2 trapping mechanisms · Plume stabilization

1 Introduction

Understanding the hydrodynamic behavior of large-volume CO_2 plumes is critical for advancing the technology of geologic carbon storage in deep saline formations. This behavior is examined by developing a numerical model of the subsurface at the proposed Kimberlina

C. Doughty (✉)
Earth Sciences Division, Lawrence Berkeley National Laboratory, University of California, Berkeley, CA 94720, USA
e-mail: cadoughty@lbl.gov

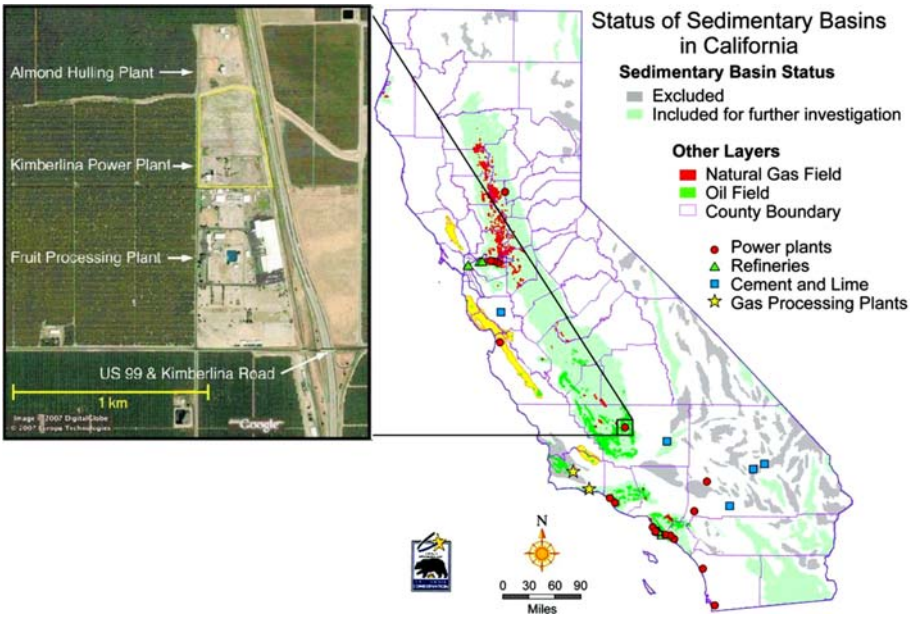

Fig. 1 Map of California showing potential geologic carbon storage sites in sedimentary basins (light green shading), courtesy of the California Energy Commission. The Kimberlina pilot test is located in the Southern San Joaquin Valley (boxed red dot). The inset shows a satellite image of the Kimberlina power plant site. The power plant and the injection well will be located near one another in the southwestern corner of the property

advanced oxy-combustion power plant with CO_2 capture in the southern San Joaquin Valley, California (Fig. 1). For its first 4 years of operation, the power plant will provide 250,000 metric tons of CO_2 per year for a large-volume CO_2 geologic storage pilot. Thereafter, the captured CO_2 will be sold locally for enhanced oil recovery operations. As shown in Fig. 1, the sedimentary basin that forms California's Central Valley provides a huge potential capacity for geologic carbon storage; thus, lessons learned from the Kimberlina site may be widely applicable.

The target storage formation is a high-permeability sand layer located at a depth of 2 km, which is over- and underlain by low-permeability shales. Within the formation itself, sands and shales are interleaved in a lenticular fashion. This geological setting provides an ideal situation for examining the interplay of buoyancy flow, capillary forces, CO_2 dissolution, and geologic heterogeneity in controlling the behavior of the injected CO_2 plume. The model simulates the 4-year injection period, in which a total of 1 million metric tons of CO_2 are injected, and the subsequent evolution of the CO_2 plume for hundreds of years. Because specific geologic information at the site of the proposed injection well is lacking (the nearest well penetrating the storage formation is 2.5 km away), the simulation results should not be taken as precise predictions, but rather general indications of the key features of CO_2 plume behavior.

In the subsurface, CO_2 exists as an immiscible free phase and as a solute in the aqueous phase. For typical hydrostatic pressure gradients and geothermal temperature gradients, free-phase CO_2 is supercritical at depths greater than about 800 m. The present study does not consider pressure/temperature conditions below the critical point of CO_2 (73.8 bars, 31°C), so CO_2 never exists as a free phase in liquid or gaseous form. Supercritical CO_2 is lighter

and much less viscous than the native brine; hence, in a two-phase flow context, it is referred to as gas, whereas the aqueous phase is referred to as liquid.

Trapping CO_2 is a significant challenge because the low density of free-phase CO_2 compared to native brine makes it strongly buoyant. Immobilizing CO_2 in the subsurface for long-term geologic storage can be accomplished by four primary mechanisms. (1) Stratigraphic or structural trapping: buoyant free-phase CO_2 is trapped beneath low-permeability layers or faults or in anticline structures. (2) Residual CO_2 trapping (also known as capillary trapping, mobility trapping, or phase trapping): multiphase flow processes immobilize free-phase CO_2. In the petroleum literature (e.g., Land 1968; Holtz 2002) it is commonly assumed that residual gas saturation (the saturation below which CO_2 is immobile) is history-dependent, with a zero or small value during the drainage process (CO_2 displacing brine), and a potentially large value during imbibition (brine displacing CO_2), which increases as the maximum historical gas saturation increases. (3) Dissolution trapping (also known as solubility trapping): the CO_2 that dissolves in brine is no longer buoyant so there is no driving force toward the surface. In fact, CO_2-saturated brine is denser than native brine. As CO_2-laden brine sinks deeper into the formation, it can set up circulation patterns that enable more free-phase CO_2 to come into contact with native brine, enabling more dissolution to occur (Ennis-King and Paterson 2005; Pruess and Zhang 2008). (4) Mineral trapping: CO_2 reacts with rock minerals to form carbonate compounds, typically over very long time scales (Pruess et al. 2003; Xu et al. 2003, 2005; Gherardi et al. 2007). The first three mechanisms, collectively referred to as hydrodynamic trapping by Bachu et al. (1994), dominate plume behavior over the hundred-year time scale and are the focus of the present paper. Because trapping mechanisms are scale-dependent, understanding large-volume pilots is a necessary step between existing studies involving small-scale CO_2 injection tests and actual commercial CO_2 storage operations. Additionally, predicting the spatial and temporal evolution of the CO_2 plume and the attendant pressure increase can help optimize design of the monitoring methods used for the pilot.

2 Model Development

2.1 Numerical Simulator

Numerical modeling is conducted using TOUGH2 (Pruess et al. 1999), a general-purpose numerical simulator for multiphase, multicomponent fluid and heat flow in porous and fractured media. TOUGH2 incorporates accurate phase-partitioning and thermophysical properties of all fluid phases and components and uses a multiphase extension of Darcy's law that includes relative permeability and capillary-pressure effects. The present studies utilize an equation of state package called ECO2N (Pruess and Spycher 2007; Spycher and Pruess 2005), designed to treat a two-phase (liquid, gas), three-component (water, salt (NaCl), CO_2) system in pressure/temperature regimes above the critical point of CO_2 ($P = 73.8$ bars, $T = 31°C$), and a hysteretic formulation for capillary pressure and relative permeability (Doughty 2007). Chemical reactions among CO_2, brine, and rock minerals are not considered in TOUGH2, but a companion code, TOUGHREACT (Xu et al. 2006), is available for such studies.

In TOUGH2, dissolution of both CO_2 and NaCl in the aqueous phase is modeled as an equilibrium process. That is, in any grid block where one or both of these components exist, there is instantaneous partitioning between the aqueous phase (dissolution) and the free phase (supercritical for CO_2 and solid for NaCl). Partitioning is controlled by the solubility of each

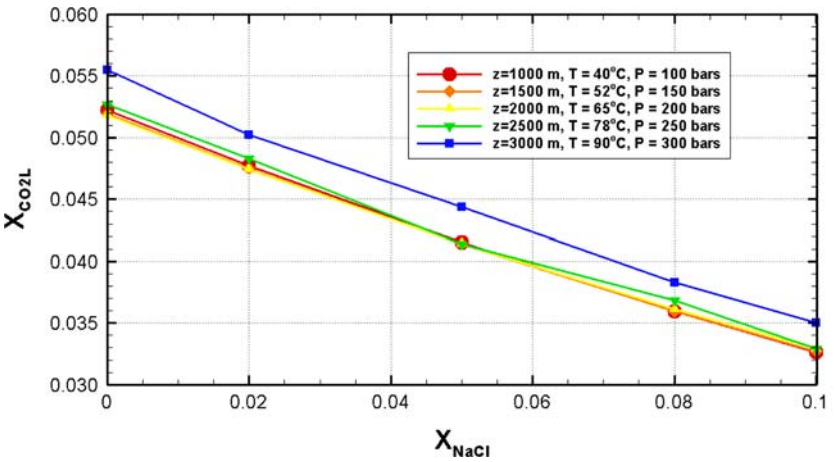

Fig. 2 CO_2 solubility (plotted as mass fraction of CO_2 in the aqueous phase) as a function of salinity (plotted as mass fraction of NaCl in the aqueous phase) for various depths, assuming a hydrostatic pressure gradient $P(z) = 1 + 0.1\ z$ and a geothermal temperature gradient $T(z) = 15 + 0.025z$

component in the aqueous phase. NaCl solubility depends only on temperature, whereas CO_2 solubility depends on temperature, pressure, and salinity, as illustrated in Fig. 2 for typical CO_2 storage conditions. CO_2 solubility increases with increasing pressure and decreases with increasing temperature and salinity. Because pressure and temperature are usually correlated, both increasing with depth, their effect on CO_2 solubility tends to cancel out, leaving salinity as the primary controlling factor.

If the amounts of CO_2 and NaCl in a given grid block are each below their respective solubility, then no free phase exists. If the amount of NaCl exceeds its solubility (e.g., as the grid block dries out), then solid salt precipitates. If the amount of CO_2 exceeds its solubility (e.g., as CO_2 is injected), then a supercritical phase develops. An important distinction between these two free phases is that solid salt is always immobile, whereas supercritical CO_2 may be mobile or immobile. Additionally, a small amount of liquid water evaporates into the supercritical phase, whereas the solid phase is pure NaCl. The fraction of pore space occupied by each phase is the saturation S, with S_g denoting the supercritical phase (primarily CO_2, with a small amount of water vapour), S_l denoting the aqueous phase (primarily water, with dissolved CO_2 and NaCl), and S_s denoting the solid salt precipitate. For each grid block, $S_g + S_l + S_s = 1$.

Together, capillary pressure P_c, liquid relative permeability k_{rl}, and gas relative permeability k_{rg} variation as a function of saturation are known as characteristic curves; they control the way the brine (the wetting phase, also called the liquid phase) and supercritical CO_2 (the non-wetting phase, also called the gas phase) interact. In a hysteretic formulation, P_c, k_{rl}, and k_{rg} depend not only on the saturation of the grid block, but also on the history of the saturation of the grid block. When gas saturation S_g increases because more CO_2 enters a grid block than leaves it, the process is known as drainage. Alternatively, when liquid saturation S_l increases because more brine enters a grid block than leaves it, the process is known as imbibition. The most critical parameter of the characteristic curves is the residual gas saturation, denoted as S_{gr}^{Δ}, which is the saturation below which gas is immobile (i.e., the saturation below which immiscible CO_2 is trapped). TOUGH2 uses the conceptualization common in the petroleum literature (Land 1968) in which it is assumed that under drainage conditions,

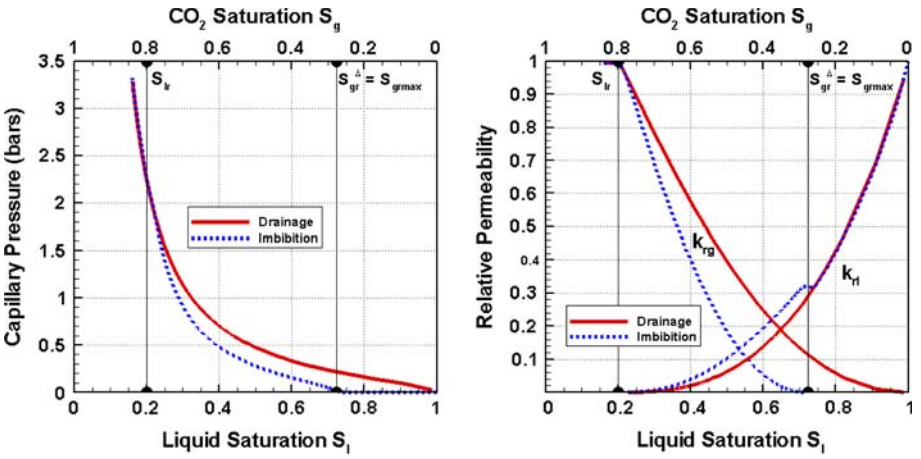

Fig. 3 Capillary pressure and relative permeabilities as a function of saturation for primary drainage and for imbibition when $S_{gr}^{\Delta}=S_{grmax}$. Smaller values of S_{gr}^{Δ} would produce curves within the envelope formed by these two curves. The curve labeled k_{rg} shows relative permeability for supercritical CO_2 and the curve labeled k_{rl} shows relative permeability for brine

$S_{gr}^{\Delta} = 0$, but for imbibition, S_{gr}^{Δ} increases as maximum historical gas saturation increases. Thus, grid blocks that once contained the most CO_2 are those which trap the most CO_2. The maximum value of S_{gr}^{Δ}, known as S_{grmax}, is a material property dependent on rock porosity (Holtz 2002). Figure 3 shows the capillary pressure and relative permeability curves under primary drainage conditions and for imbibition when $S_{gr}^{\Delta} = S_{grmax}$. Smaller values of S_{gr}^{Δ} would produce curves within the envelope formed by these two curves. Figure 3 illustrates that CO_2 mobility can be much smaller under imbibition than under drainage.

During a CO_2 injection period, drainage is the dominant process because the CO_2 plume is growing in all directions; hence $S_{gr}^{\Delta}= 0$ and no CO_2 is trapped as residual gas. After injection ends, the leading edge of the CO_2 plume may still undergo drainage as the plume moves upward and up-dip by buoyancy forces, but at the trailing edge of the plume imbibition occurs, $S_{gr}^{\Delta} >> 0$, and a significant fraction of the CO_2 plume may be trapped as residual gas.

Although TOUGH2 has the capability of solving fully coupled fluid and heat flow problems, temperature is assumed to remain constant for the present simulations, to increase computational efficiency. Previous studies (Doughty and Myer 2009) have shown that thermal effects of CO_2 injection are minor if the injected CO_2 is pre-heated to near in situ temperature. Additionally, the slow flow process of aqueous-phase diffusion of dissolved species is not included in these simulations. For a typical CO_2 diffusivity of $D = 2{\cdot}10^{-9}\mathrm{m}^2/\mathrm{s}$ (Pruess and Zhang 2008), the characteristic diffusion length $(Dt)^{1/2}$ is only 0. 5 m for 4 years, 2.5 m for 100 years, and 8 m for 1,000 years, all small compared to CO_2 plume dimensions. Finally, TOUGH2 has the capability to decrease intrinsic permeability due to salt precipitation, but it is not invoked for the present simulations because the amount of salt that precipitates is small.

2.2 Geologic and Facies Models

A geologic model of the Southern San Joaquin Valley surrounding the Kimberlina power plant (Wagoner 2009) is shown in Fig. 4. The target CO_2 storage formation is the Vedder

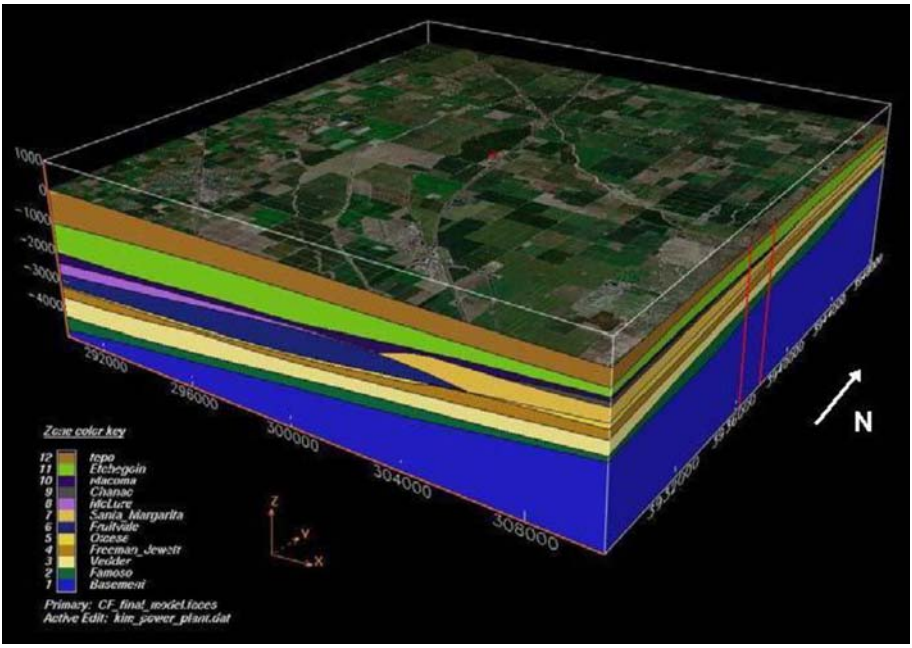

Fig. 4 Geologic model of the southern San Joaquin Valley (adapted from Wagoner 2009). The location of the Kimberlina power plant is shown by the red dot near the center

Formation, a lower Miocene, fine- to coarse-grained massive marine sandstone with subordinate siltstone and shale. At the Kimberlina site, the Vedder Formation depth is 2 km, and its thickness is about 160 m. The overlying Freeman–Jewett Formation, a 100-m thick lower Miocene marine shale and siltstone, provides the upper seal.

A facies model of the Vedder Formation surrounding the Kimberlina site (J. Wagoner, personal communication, 2007) provides the basis for the TOUGH2 model. The facies model (Fig. 5) is centered at the proposed Kimberlina power plant and covers an area of 125 km^2. Over the entire model area, Vedder Formation thickness ranges from 110 m to 187 m, but within the 2 km surrounding the power plant, thickness only ranges from 150 m to 164 m. The Vedder Formation dips 7° to the WSW.

The facies model uses 180 layers, of equal thickness, to represent the Vedder Formation. Each layer contains 2,500 cells: 50 cells each 250 m wide in the E–W (x) direction by 50 cells each 200 m long in the N–S (y) direction. A facies (either sand or shale) is assigned to each cell, by interpolating sand/shale picks obtained from eight well logs. Because of the limited information available from such a small number of wells, no attempt is made to represent heterogeneity within the individual facies. Overall, the facies model contains about 50% sand and 50% shale, interleaved in a lenticular fashion, with typical lens size 15 m thick and several kilometers in lateral extent. At the location of the proposed injection well, the Vedder Formation is 158 m thick and consists of five sand layers with total thickness 79 m, separated by four shale lenses with total thickness 79 m.

2.3 Numerical Model

The TOUGH2 model (Fig. 6) covers roughly the same spatial extent as the facies model. Because the formation dip and thickness are nearly uniform in the vicinity of the power plant

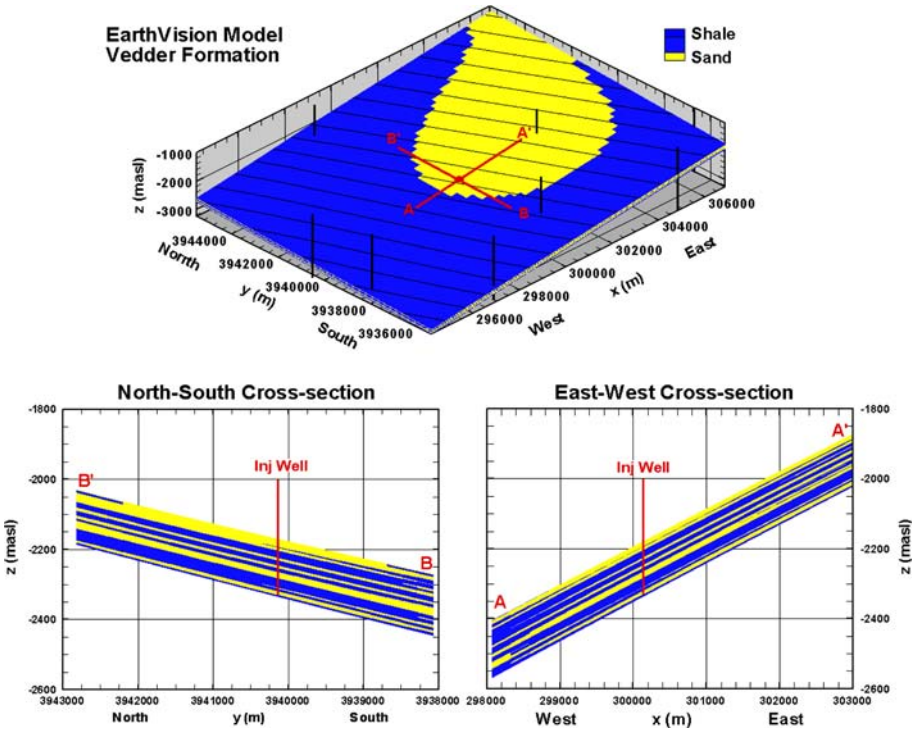

Fig. 5 Three views of the facies model of the Vedder Formation. The perspective view (top) has no vertical exaggeration, whereas the two cross sections (bottom) have five times vertical exaggeration, to enable sand/shale layering to be seen. In the perspective view, the thick black line segments show the locations of the eight wells used to develop the facies model, the thin black lines are depth contours, and the intersection of the two cross sections marks the location of the injection well in the TOUGH2 simulations

(note that depth contour lines in the perspective view of Fig. 5 are essentially equidistant and linear), the TOUGH2 model is constructed as a tilted plane, with just a single value of thickness (157.5 m) and dip (7°). The up-dip direction is 30° counter-clockwise from the $+x$-axis (ENE), corresponding to the WSW down-dip direction. Each TOUGH2-model layer is formed by combining six facies-model layers, resulting in 30 layers, each 5.25 m thick. At the (x, y) location of each facies-model cell, the facies of the TOUGH2-model layer is taken to be the facies that occurs the most times among the six facies-model layers that are combined to form it. As can be seen by comparing Figs. 5 and 6, this combining scheme captures the essential features of the lenticular sand/shale structure of the facies model.

The computational grid for the TOUGH2 model is shown in Fig. 7. Laterally, the TOUGH2 model grid-block size varies, with finest grid blocks in the vicinity of the injection well (5 m × 5 m), increasing to 55 m × 55 m in the region where the CO_2 plume is expected to go (roughly an ellipse with a major axis <2 km), and gradually increasing further beyond that region. The lateral extent of the active portion of the TOUGH2 model is 11 km × 11 km, beyond which additional grid blocks are added to represent lateral boundary conditions. The vertical discretization of the TOUGH2 model into 30 layers results in at least two model layers per sand layer, to enable vertical flow arising from buoyancy forces to be resolved.

The 5-m width of the grid-block used for the injection well is much greater than an actual well diameter, so the simulation is not expected to accurately reproduce all near-wellbore

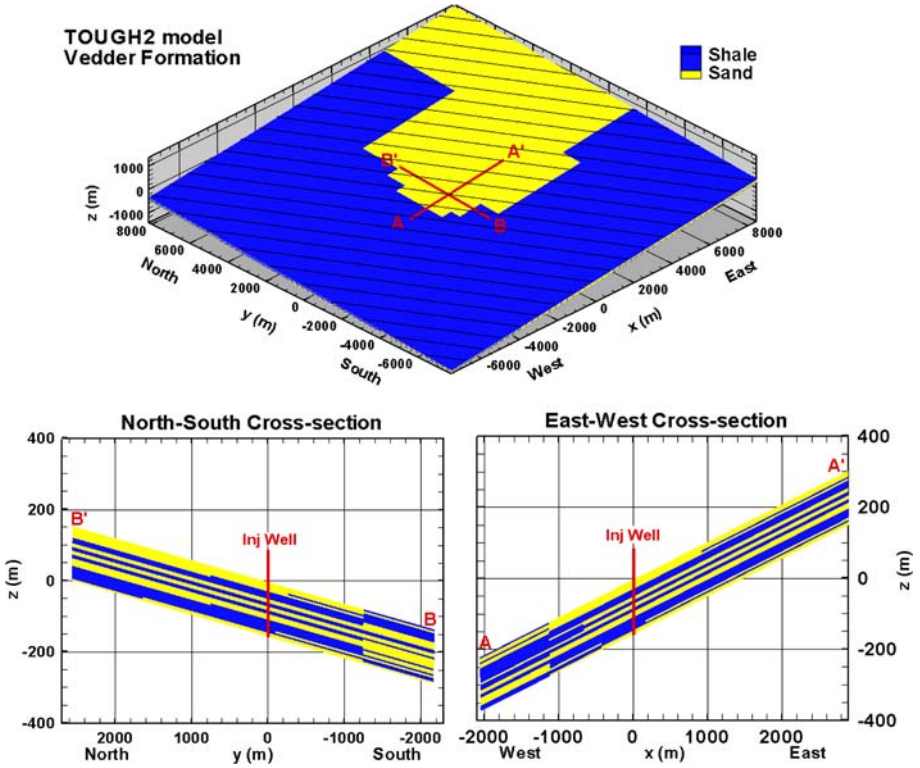

Fig. 6 Three views of the TOUGH2 model of the Vedder Formation. The perspective view (top) has no vertical exaggeration, whereas the two cross sections (bottom) have five times vertical exaggeration, to enable sand/shale layering to be seen. In the perspective view, the thin black lines are depth contours, and the intersection of the two cross sections marks the location of the injection well in the TOUGH2 simulations. Note that the coordinate system has been translated so that the origin is where the injection well intersects the top of the Vedder Formation

effects arising during CO_2 injection. For example, the modeled pressure increase will not be the actual pressure increase in the wellbore, but an average over 5 m of formation surrounding the well. However, the focus of the present paper is on plume-scale effects, and using a grid fine enough to represent an actual wellbore would greatly slow down the simulations. Two features that are not included in the present simulations, thermal effects and intrinsic permeability decrease due to salt precipitation, have their main effect within or close to the wellbore, so neglecting them is consistent with the use of the present grid.

The top and bottom boundary of the TOUGH2 model are no-flow boundaries, to represent regionally extensive, continuous shale layers over- and underlying the Vedder Formation. In the x-direction, the lateral boundaries are constant pressure boundaries and in the y-direction the lateral boundaries are no-flow boundaries. These boundary conditions are chosen for numerical convenience rather than geological accuracy. The actual extent of the Vedder Formation is estimated to be 55 km in the east–west direction and 90 km in the north-south direction, far beyond the lateral extent of the TOUGH2 model. As shown in the "simulation results" section, the lateral boundaries are so far away from the injection well and the region the CO_2 plume occupies that they have little impact on the evolution of the CO_2 plume. Table 1 summarizes the geometric properties and boundary conditions of the TOUGH2 model.

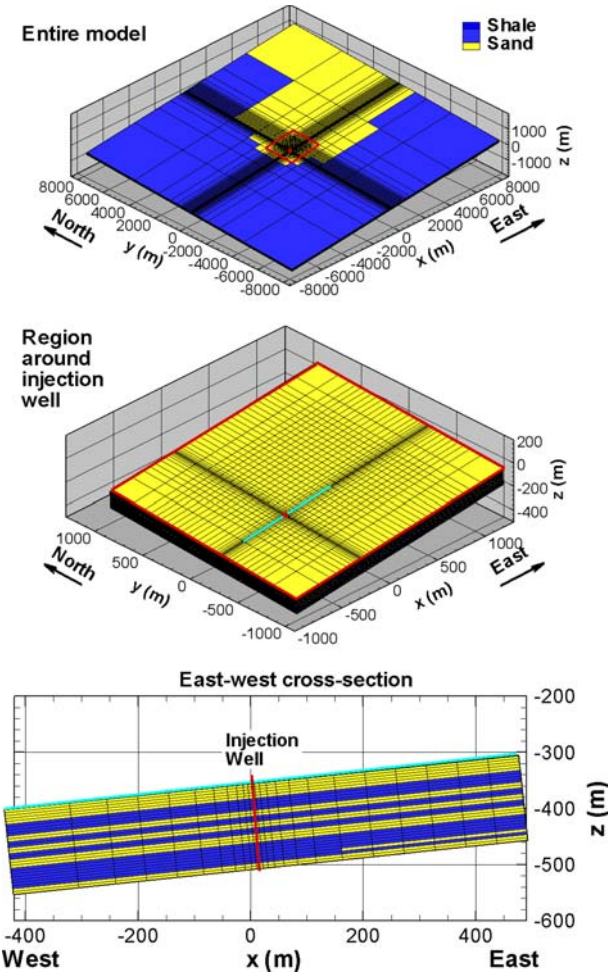

Fig. 7 Three views of the TOUGH2 model of the Vedder Formation showing the computational grid

The initial conditions for the CO_2 injection are a brine-saturated formation with a hydrostatic pressure distribution, and a pressure of 220 bars at the injection well location. Initial temperature and salinity are uniform at 81°C and 50,000 TDS, respectively. This temperature is calculated assuming a surface temperature of 15°C and a geothermal gradient of 30°C per km, both of which are rough estimates considered reasonable for Southern California. In the absence of specific information on salinity for the Vedder Formation, a moderate value of 50,000 TDS is chosen. The primary impact of the initial pressure and temperature is to define the density and viscosity of the CO_2 plume in the subsurface. Density controls not only the volume of the plume, but also the strength of the buoyancy force, which is proportional to the density difference between injected CO_2 and native brine. In conjunction with permeability, viscosity controls how mobile the CO_2 is. The effects of initial pressure and temperature on plume migration are examined elsewhere (Jordan and Doughty 2008). According to Fig. 2, salinity is inversely related to CO_2 solubility. If actual salinity turns out to be lower than 50,000 TDS (values as low as 20,000 TDS have been proposed), a greater fraction of the

Table 1 Geometric properties and boundary conditions of the TOUGH2 model for the Vedder Formation at the Kimberlina power plant site

Parameter	Value	Comment
Depth at injection well (m)	2,200	Same as facies model
Thickness (m)	157.5	Facies model thickness ranges from 110 m to 187 m
Percent sand/shale	50/50	Sand occurs in five distinct layers, with interleaving shales
Number of model layers	30	Each model layer 5.25 m thick, combines 6 facies-model layers
Lateral extent (km)	11 × 11	Comparable to facies model
Lateral grid spacing	Varies	5 m × 5 m at injection well; maximum 55 m × 55 m within CO_2 plume footprint
Formation dip	7°	Up-dip direction is ENE, 30° counter-clockwise from $+x$-axis
Boundary Conditions		
Top and bottom	No flow	Represent continuous, extensive shale layers
Lateral, x-direction	Constant pressure	
Lateral, y-direction	No flow	

Table 2 Initial conditions and flow properties of CO_2 and brine

Initial condition	Value	
Initial pressure	Hydrostatic pressure distribution; average 220 bars at injection well	
Initial temperature	81°C	
Initial salinity	50,000 mg/L	
CO_2 solubility in brine	43,000 mg/L	
Flow property	CO_2	*Brine*
Density (kg/m^3)	632	1,014
Viscosity (Pa-s)	$5 \cdot 10^{-5}$	$4 \cdot 10^{-4}$

injected CO_2 will dissolve and the free-phase plume will be correspondingly smaller. Additionally, lower salinity means smaller brine density, which decreases the driving force for buoyant flow of free-phase CO_2. Thus, the present simulation results may be considered to be conservative in terms of predicting plume extent and migration. Table 2 summarizes the initial conditions used for the Kimberlina simulations, and the resulting density and viscosity of the injected CO_2 and the native brine. It shows that the injected plume will be strongly buoyant in the subsurface.

The material properties used in the base-case TOUGH2 model are summarized in Table 3. Porosity and permeability values are consistent with the geologic model, but relative permeability and capillary pressure parameters are not known for the Kimberlina site, so parameter values are adapted from other studies of CO_2 geologic storage in saline formations (Doughty 2007; Doughty et al. 2008). Sensitivity studies then examine the impact of varying permeability, permeability anisotropy (both vertical and lateral), and maximum residual gas saturation. Table 3 shows that the permeability contrast between the sand and shale facies is large; thus CO_2, which is injected only into sand layers, is expected to remain in the sand layers. The functional forms of the hysteretic characteristic curves (Doughty 2007) are based on the van Genuchten (1980) formulation.

Table 3 Material properties of the base-case TOUGH2 model

Property	Sand	Shale
Porosity	28%	15%
Horizontal[a] permeability, k_x, k_y	200 md	0.1 md
Vertical[a] permeability k_z	20 md	0.01 md
Relative permeability parameters		
Residual liquid saturation S_{lr}	0.2	0.3
Maximum residual gas saturation S^{b}_{grmax}	0.27	0.29
van Genuchten parameter m	0.917	0.917
Capillary pressure parameters (same for drainage and imbibition branches)		
Capillary pressure strength P_{c0}	$1.88 \cdot 10^4$ Pa	$8.41 \cdot 10^5$ Pa
van Genuchten parameter m	0.412	0.412

[a] "Horizontal" means parallel to layering; "vertical" means perpendicular to layering
[b] Residual gas saturation S^{Δ}_{gr} is zero during drainage and non-zero during imbibition, where it depends on saturation history and has a maximum value of S_{grmax}

The CO_2 injection well is located at the center of the model and penetrates the entire Vedder Formation thickness. Because the TOUGH2 model does not include an actual wellbore model (recall that lateral grid spacing at the injection well location is 5 m × 5 m), injection is modeled as a mass source distributed among the sand layers, with source strength proportional to layer thickness. Altogether, 250,000 T/year is injected for a period of 4 years, resulting in 1,000,000 metric tons of CO_2 injected.

3 Simulation Results

The TOUGH2 simulations cover the 4-year injection period and at least 100 years thereafter, when CO_2 is subject only to gravity and capillary forces. All simulations use the computational grid as shown in Fig. 6 and the properties shown in Tables 1 and 2. Base-case simulations use the properties as shown in Table 3, while sensitivity studies consider alternative values whose ranges reflect the uncertainty of our knowledge of actual properties.

3.1 Base Case

3.1.1 Supercritical CO_2

Figures 8 and 9 show snapshots of the supercritical CO_2 plume at various times. Figure 8 shows a plan view of the uppermost layer of the model, which is the layer in which the greatest lateral extent of CO_2 occurs. Figure 9 shows $x - z$ cross-sections through the model, and illustrates the formation of five sub-plumes in the five sand layers within the Vedder Formation. Note from Fig. 8 that the $x - z$ plane does not show the maximum lateral extent of CO_2, which occurs in the up-dip direction. Together, Figs. 8 and 9 illustrate the strong buoyancy flow that moves CO_2 to the top of each sand layer, and from there moves the plume up-dip.

Key measures of the CO_2 plume are its up-dip extent at stabilization and the time evolution of the partitioning of CO_2 between dissolved, immobile-gas, and mobile-gas forms. In the present study, plume stabilization is defined as occurring when two successive snapshots show no advance of the leading edge of the plume. Figure 8 shows that the base-case plume

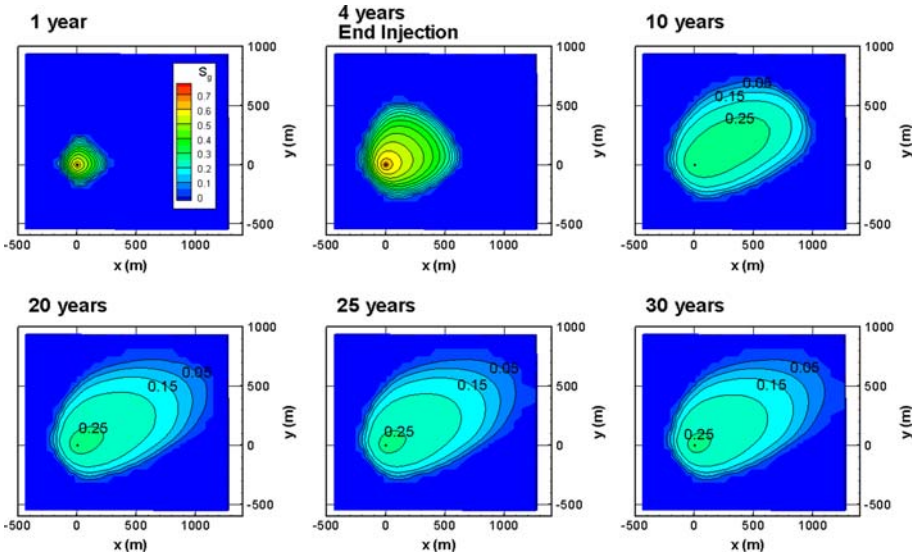

Fig. 8 Top view of the base-case supercritical CO_2 plume at a series of times, shown by plotting S_g, saturation of supercritical CO_2, in the uppermost model layer. During injection, the rectilinear grid produces minor numerical artifacts in the plume distribution by enabling enhanced flow along the grid axis directions

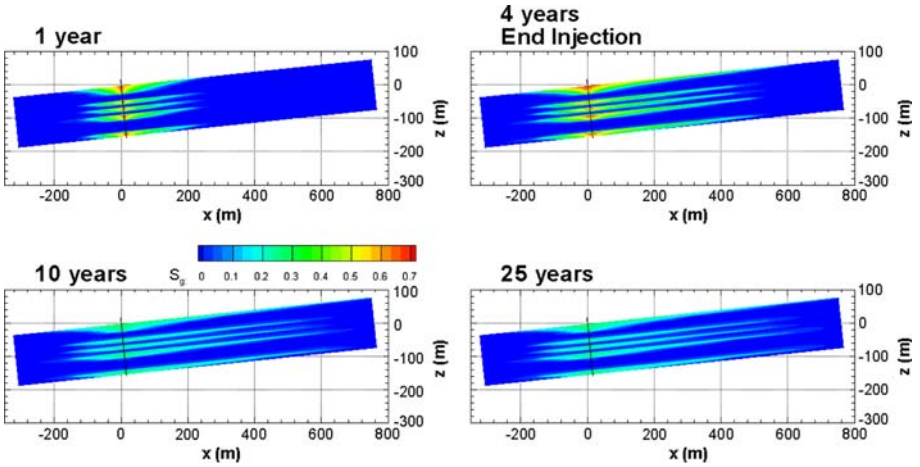

Fig. 9 East–west cross section of the base-case supercritical CO_2 plume at a series of times, shown by plotting S_g, saturation of supercritical CO_2, in the plane $y = 0$

has stabilized by 25 years, at which time it is about 1,500 m long, 900 m wide, and extends 1,300 m up-dip of the injection well.

Quantification of the trapping and stabilization process is presented in Fig. 10, which shows the time evolution of the CO_2 mass distribution for the entire model. The total amount of CO_2 injected is divided into two parts, i.e., a gas-like supercritical phase and a dissolved phase. The supercritical phase is further divided into mobile and immobile portions, with CO_2 immobile when its saturation is below residual gas saturation S_{gr}^{Δ}. Throughout the injection period, about 20% of the CO_2 dissolves, and essentially all the supercritical-phase

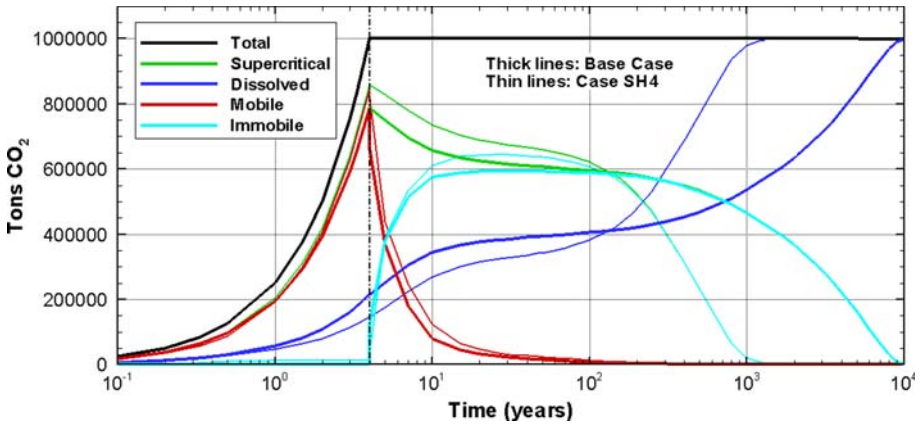

Fig. 10 Time evolution of the CO_2 mass distribution for the entire model for the base-case (thick lines) and sensitivity-study case SH4, which models the Vedder Formation as a homogeneous, isotropic sand (thin lines)

CO_2 is mobile. After injection ends, the dissolved fraction increases gradually to 38% as the plume moves up-dip and encounters new under-saturated brine. This up-dip movement is accompanied by residual CO_2 trapping, and Fig. 10 shows how the mobile fraction of supercritical CO_2 decreases concurrent with the increase of the immobile fraction. By 25 years the supercritical CO_2 is largely immobile, coinciding with the stabilization of the plume as shown in Fig. 8. Thereafter, the plume does not move as a whole, but subtle redistributions of the immiscible phase further decrease the mobile fraction and dissolution of supercritical CO_2 continues, slowly increasing the dissolved fraction. The supercritical plume has nearly completely dissolved by 10,000 years.

Insight into residual CO_2 trapping can be obtained by examining the spatial distribution of drainage and imbibition at a series of times during and after injection. Figure 11 displays ICURV, the variable identifying which branch of the capillary pressure curve is being followed, for each grid block in the uppermost model layer. Recall that residual CO_2 trapping requires a non-zero value of residual gas saturation, which only occurs during imbibition. Nearly the entire plume is undergoing drainage just after the injection period ends, except for a narrow imbibition zone at the trailing (down-dip) edge of the plume. The imbibition zone grows steadily until 25 years, when drainage is limited to a few grid blocks at the leading (up-dip) edge of the plume, at which time the plume has stabilized. Thereafter, the zone of drainage gradually shrinks further, until it has disappeared by 100 years.

Because imbibition dominates the plume for most of the post-injection period, the residual gas saturation S_{gr}^{Δ} is non-zero over much of the plume (Fig. 12), enabling significant residual CO_2 trapping. The S_{gr}^{Δ} distribution does not change after the plume stabilizes at 25 years.

Figure 13 shows the spatial distribution of $(S_g - S_{gr}^{\Delta})$, the difference between gas saturation and residual gas saturation. The larger the value of $(S_g - S_{gr}^{\Delta})$, the more mobile the plume is (Fig. 3). There is a sharp decrease in mobility at the transition from drainage ($S_{gr}^{\Delta} = 0$) to imbibition ($S_{gr}^{\Delta} > 0$) at 4, 5, and 7 years (compare to Figs. 11 and 12). From 10 years on, $(S_g - S_{gr}^{\Delta})$ is very small throughout the plume. Beginning at 20 years, negative values of $(S_g - S_{gr}^{\Delta})$ develop, which can only happen if immobile free-phase CO_2 is dissolving. Continued dissolution of immobile CO_2 implies that the brine must be moving, because quiescent brine adjacent to immobile free-phase CO_2 would quickly saturate, precluding further

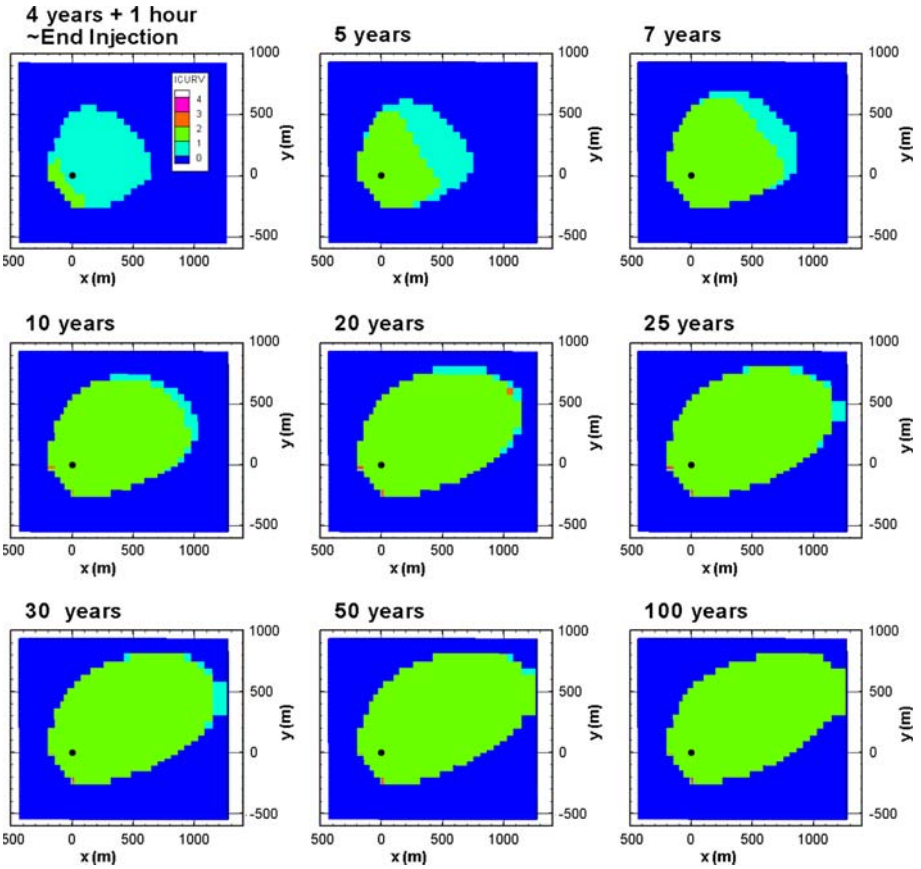

Fig. 11 Top view of base-case distribution of drainage and imbibition at a series of times: ICURV = 0—single-phase liquid, 1—primary drainage, 2—first-order imbibition, 3—second-order drainage, and 4—third-order imbibition

dissolution. The present simulations do not include regional groundwater flow, so the only driving force for brine movement is natural convection, arising from the small brine density increase that occurs when CO_2 dissolves. The banded character of the negative $(S_g - S_{gr}^{\Delta})$ values evident at 500 and 1,000 years suggests the formation of convection cells in the brine underlying the free-phase CO_2, with the top of each cell (where lighter CO_2-free native brine up-wells) coincident with a band of enhanced dissolution.

3.1.2 Dissolved CO_2

Before investigating the natural convection of CO_2-laden brine, it is worthwhile to examine further how the free-phase CO_2 and dissolved CO_2 interact. Figure 14 shows a vertical cross-section of the storage formation in the vicinity of the injection well at 4 years, the end of the injection period. The top frame shows free-phase CO_2, the second frame shows CO_2 dissolved in the brine, the third frame shows the NaCl dissolved in the brine, and the bottom frame shows precipitated NaCl. Dissolved species are shown as mass fractions in

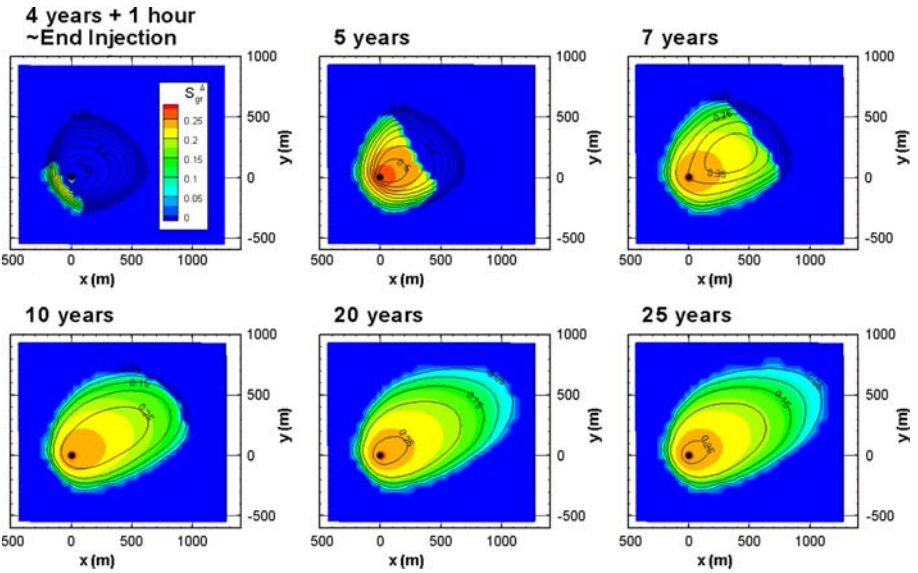

Fig. 12 Top view of base-case distribution of residual gas saturation S_{gr}^{Δ} at a series of times (colors). Contour lines show supercritical CO_2 saturation S_g, illustrating the spatial distribution of the plume itself

the aqueous phase, whereas precipitated NaCl is shown as solid saturation S_s (i.e., the pore volume fraction of precipitated NaCl).

For the most part, the spatial distribution of dissolved CO_2 coincides with that of free-phase CO_2. The one exception is close to the injection intervals where S_g is large. In these locations, strong capillary forces arising from large values of S_g draw brine toward the well. Near the well, some of the water evaporates into the supercritical CO_2 phase, increasing dissolved NaCl content in the remaining brine. There is an inverse correlation between NaCl content and CO_2 solubility (Fig. 2), resulting in the regions of low dissolved CO_2 near the injection intervals. Otherwise, the close correspondence between the spatial extents of free-phase and dissolved CO_2 indicates that natural convection of brine is negligible at this time. Recall that aqueous-phase diffusion is not included in these simulations. The slight extension of the dissolved-CO_2 plume beyond the free-phase plume visible in Fig. 14 is likely due to numerical dispersion.

Figure 15 shows dissolved CO_2 distributions at 25, 100, and 500 years. With time, spatial distributions of dissolved and free-phase CO_2 increasingly differ, confirming that natural convection of CO_2-laden brine is significant, and the convection cells themselves are illustrated by the irregular distribution of dissolved CO_2 in the up-dip region of the top sand layer at 100 and 500 years. The low-permeability shales separating each of the five sub-plumes, constrain the bulk of the brine flow to the sand layers. Flow is greater down-dip, but up-dip flow into the deeper parts of each sand layer is also evident. At times beyond 500 years (not shown), down-dip migration of dissolved CO_2 continues, but its up-dip extent does not change appreciably. At the final simulation time (10,000 years) the dissolved CO_2 plume extends about 4 km down-dip from the injection well.

3.1.3 Pressure Response

Figure 16 compares the lateral extent of the pressure response to CO_2 injection with the lateral extent of the CO_2 plume itself. The profiles show pressure change and gas saturation in the

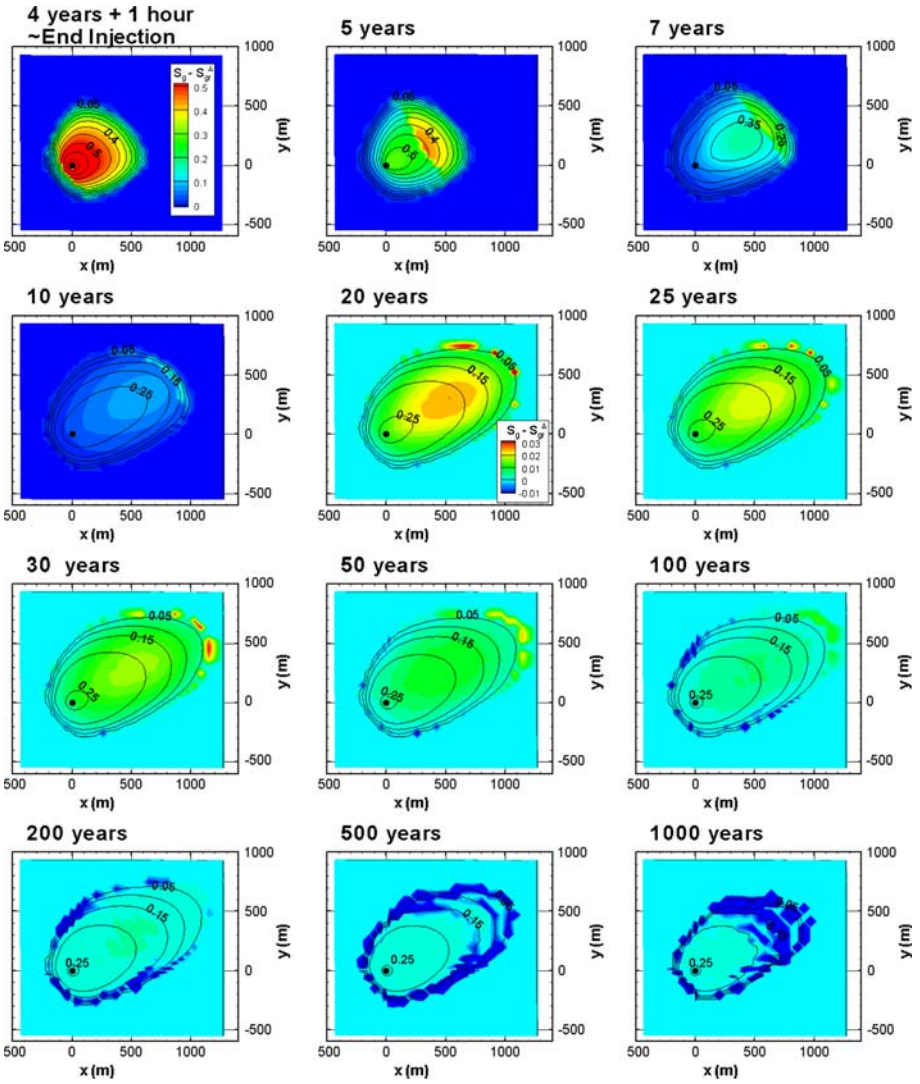

Fig. 13 Top view of base-case distribution of $(S_g - S_{gr}^{\Delta})$ at a series of times (colors). Contour lines show S_g, saturation of supercritical CO_2, illustrating the spatial distribution of the plume itself. Note that different color maps are used for the first four frames and for the final eight frames, where all negative values of $(S_g - S_{gr}^{\Delta})$ are shown in dark blue

uppermost layer in the model, along a transect beginning at the injection well and extending in the up-dip direction. During the injection period, pressure close to the injection well does not increase monotonically with time. This occurs because the viscosity of injected CO_2 is much lower than that of the native brine (Table 2), and as the CO_2 plume grows there is less resistance to flow, so less pressure increase in response to the constant CO_2 injection rate. After injection ends, CO_2 saturation decreases as the plume stretches out, with the leading edge of the CO_2 plume moving up-dip and the maximum pressure increase moving along with it. Although the pressure response extends far beyond the CO_2 plume, the pressure response

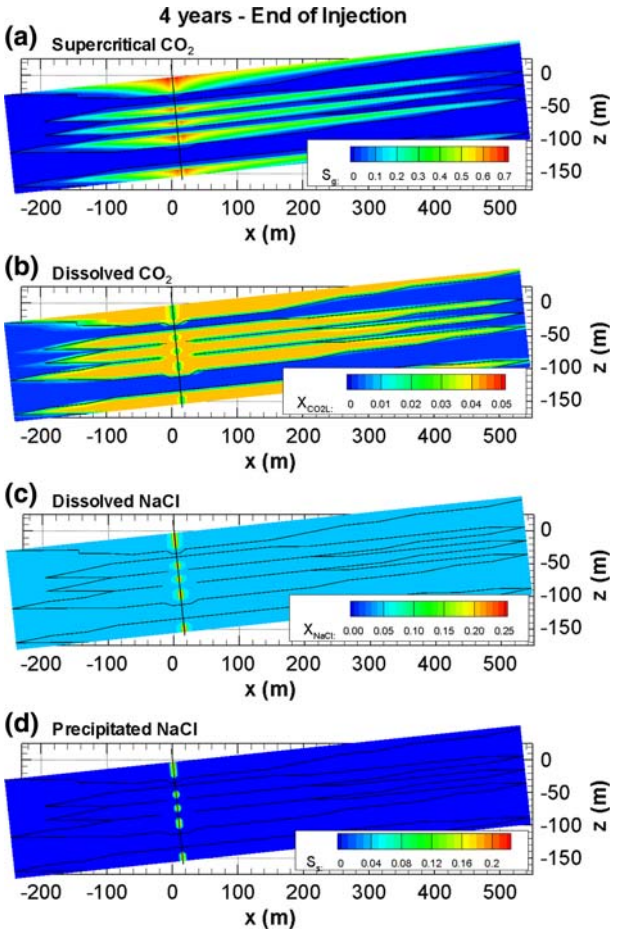

Fig. 14 East–west cross-section of the base-case plume in the plane $y = 0$ at 4 years: **a** S_g shows saturation of supercritical CO_2; **b** $X_{CO_{2L}}$ shows the mass fraction of CO_2 dissolved in the aqueous phase; **c** X_{NaCl} shows the mass fraction of NaCl dissolved in the aqueous phase; **d** S_s shows saturation of precipitated NaCl. The black contour lines show $S_g = 0$, illustrating the maximum extent of the supercritical plume

beyond the CO_2 footprint is small (<1.5 bars). Moreover, pressure response decreases as distance from the injection well increases, and quickly dissipates after injection ceases (<1 bar everywhere 1 year after injection ends).

Recall that the base-case model assumes partially open (constant-P), partially closed (no flow) boundary conditions. Two additional simulations, assuming either all-open or all-closed lateral boundary conditions, produce identical CO_2 plumes, and only slightly different pressure responses. During the injection period, pressure responses are similar for all the cases. Only near the lateral boundary does the all-closed case differ significantly, with a pressure increase of just over 0.2 bars (the pressure response at the open boundaries is guaranteed to be zero). After injection ceases, the pressure change at all distances decreases to near zero for the base case (Figure 16) and the all-open case (not shown) within 20 years. In contrast, for the closed case, the pressure change becomes uniform in space at a value just below 0.3 bars.

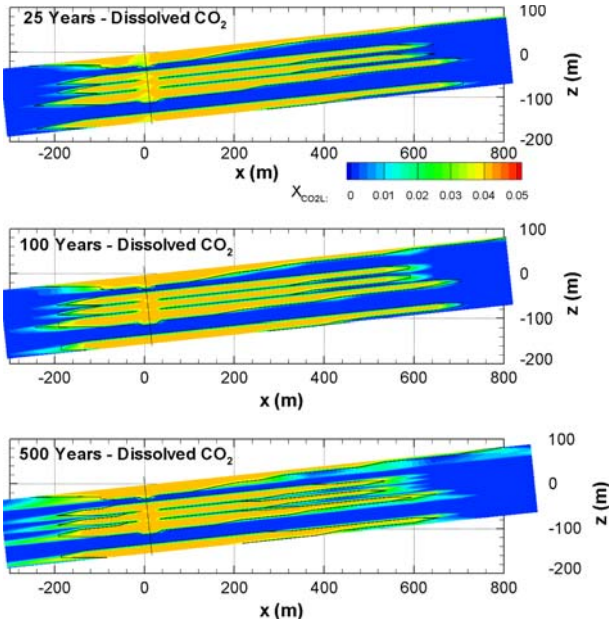

Fig. 15 Late-time (i.e., post-stabilization) distributions of base-case dissolved CO_2, shown by plotting $X_{CO_{2L}}$, the mass fraction of CO_2 dissolved in the aqueous phase, in the plane $y = 0$. The black contour lines show $S_g = 0$, illustrating the maximum extent of the supercritical plume

3.2 Sensitivity Studies

Most of the material properties used as input to the base-case numerical simulation are not well known. To assess the impact of parameter uncertainty on plume evolution and trapping mechanisms, sensitivity studies are carried out using alternative parameter choices for poorly known parameters. Table 4 summarizes the cases and the key performance measures for each. Figure 17 shows a plan view of the top of the stabilized plume for each case.

The time variation of the mass of mobile CO_2 (Fig. 10) shows an initial rapid decrease after injection ends followed by a very slow approach to zero, which does not provide a convenient means for determining when a plume has stabilized. It is clear from the time series of CO_2 distributions (Fig. 8) that the plume does not move perceptibly after 25 years, even though mobile CO_2 remains. Rather than trying to find a threshold mass of mobile CO_2 that defines stabilization, the CO_2 distributions are used directly, and stabilization is defined as occurring when two successive distributions are indistinguishable. However, it is also useful to compare among cases how long it takes to reach a given amount of mobile CO_2. The "time to 3% mobile CO_2" entry in Table 4 serves this purpose. The value of 3% is used because all the cases reach it within the simulation period (typically 100 years). Table 4 indicates that there is generally a good correlation between the "time to 3% mobile CO_2" and "time of plume stabilization" entries; therefore, they are often referred to collectively as time measures for plume mobility.

3.2.1 Sand Anisotropy Studies

The base-case model assumes that vertical permeability is 1/10th of horizontal permeability, a common assumption for sands with permeability in the hundred millidarcy range. Assuming

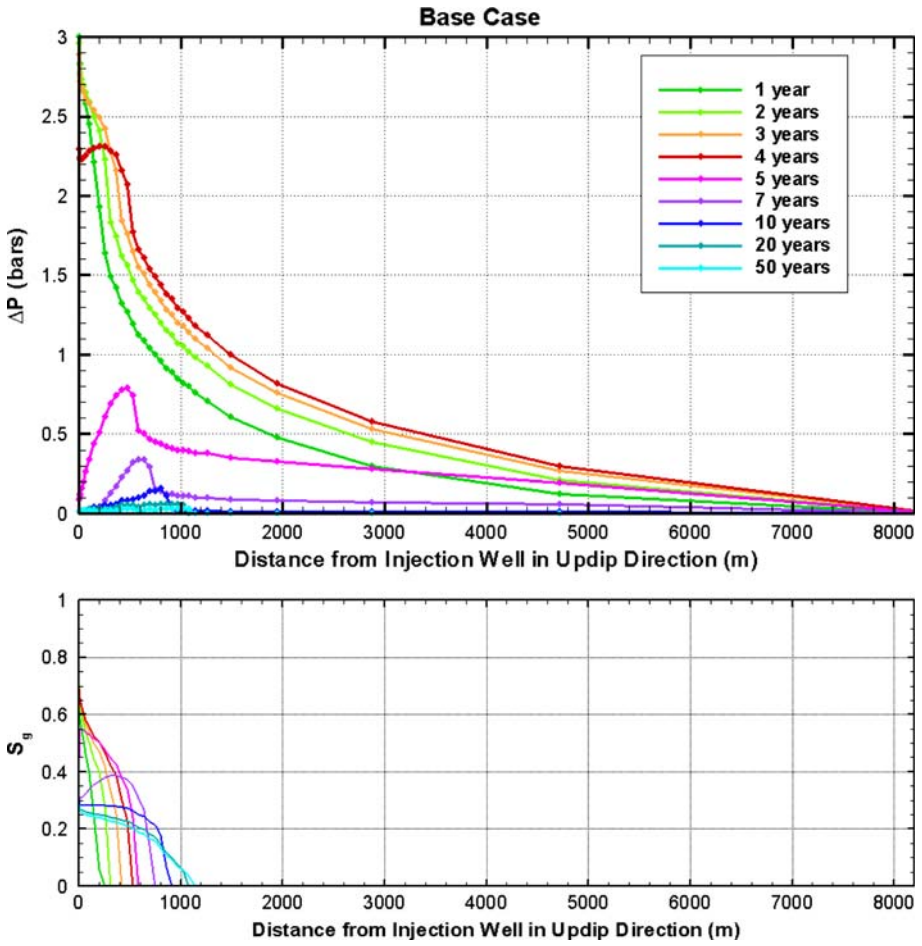

Fig. 16 Pressure change and supercritical CO_2 saturation S_g versus up-dip distance from the injection well at a series of times, for the base-case

an isotropic medium (Case AN1) produces only subtly different plume evolutions: comparable time measures for plume mobility, only 50 m more up-dip migration, and similar percent dissolved CO_2. This insensitivity largely arises from the sand/shale layering, which creates five sub-plumes in the sand layers, and thereby limits the amount of buoyancy flow that can occur. A change by a factor of ten in permeability anisotropy has a much greater effect for a homogeneous sand formation (see Cases SH3 and SH4 below).

The region surrounding the Kimberlina site contains numerous small faults trending generally north–south. Whether these faults act as conduits or barriers to flow, their net effect is likely to be a lateral (x : y) anisotropy in sand permeability with a greater permeability in the north–south (y) direction. Cases AN2 and AN3, with a 3:1 and 10:1 y : x anisotropy ratio, respectively, show that the direction of plume migration shifts dramatically from the up-dip direction (30° north of due east) toward the north. For the 10:1 anisotropy ratio, the time measures for plume mobility are shorter and up-dip plume extent and percent dissolved

Table 4 Summary of sensitivity studies

Case	Key Features	Time to 3% mobile CO_2 (years)	Time of plume stabilization (years)	Up-dip migration distance at stabilization (km)	Percent dissolved at stabilization
Base-case	$k_x = k_y$ = 200 md, k_z = 20 md, $S_{grmax} = 0.27$	23	25	1.30	38
	Sand anisotropy studies				
AN1	Isotropic permeability $k_x = k_y = k_z$ = 200 md	22	25	1.35	39
AN2	Lateral permeability anisotropy $k_x = k_y/3$, $< k_x k_y >_g$ = 200 md, k_z = 20 md	23	25	1.50	39
AN3	Lateral permeability anisotropy $k_x = k_y/10$, $< k_x k_y >_g$ = 200 md, k_z = 20 md	21	20	2.50	41
	Sand permeability studies[a]				
SA1	Very low permeability $k_x = k_y$ = 20 md, k_z = 2 md	94	85	0.70	32
SA2	Low permeability $k_x = k_y$ = 66 md, k_z = 6.6 md	37	50	1.00	34
SA3	High permeability $k_x = k_y$ = 500 md, k_z = 250 md	16	20	2.00	45
SA4	Very high permeability $k_x = k_y = k_z$ = 1,000 md	12	15	2.50	52
	Shale permeability studies[a]				
SH1	Medium-permeability shale $k_x = k_y$ = 2 md, k_z = 0.2 md	29	25	1.30	39
SH2	High-permeability shale $k_x = k_y$ = 20 md, k_z=2 md	20	40	1.50	38
SH3	No shale $k_x = k_y$ = 200 md, k_z=20 md	27	25	1.80	33
SH4	No shale $k_x = k_y = k_z$ = 200 md	32	40	2.20	33

Table 4 continued

Case	Key Features	Time to 3% mobile CO_2 (years)	Time of plume stabilization (years)	Up-dip migration distance at stabilization (km)	Percent dissolved at stabilization
	Residual gas saturation studies[b]				
SG1	High residual gas saturation $S_{grmax} = 0.40$	10	15	1.05	32
SG2	Medium-high residual gas saturation $S_{grmax} = 0.30$	19	25	1.20	37
SG3	Medium-low residual gas saturation $S_{grmax} = 0.20$	45	25	1.45	43
SG4	Low residual gas saturation $S_{grmax} = 0.10$	114	30	1.80	53

[a] When permeability decreases, capillary pressure strength P_{c0} and S_{grmax} increase

[b] Here, only S_{grmax} is varied

CO_2 are greater, which are features common to the high sand permeability cases described below.

3.2.2 Sand Permeability Studies

Sand horizontal permeability values ranging from 20 md to 1000 md are considered here (Cases SA1, SA2, SA3, and SA4). In our conceptual model, when sand permeability k increases, the vertical to horizontal permeability ratio k_z/k_x increases, capillary pressure strength P_{c0} decreases as $P_{c0} \sim k^{-1/2}$, and maximum residual gas saturation S_{grmax} decreases as $S_{grmax} = 0.48 - 0.04 \ln(k)$, with k in md, which is adapted from correlations developed by (Holtz, 2002, personal communication, 2003), based on Gulf Coast sandstone literature.

Increasing sand permeability has a strong effect on the plume performance measures shown in Table 4, with up-dip plume extent and percentage of dissolved CO_2 increasing, whereas time measures for plume stability and maximum CO_2 saturation decrease. All these effects are a consequence of the greater buoyancy flow enabled by larger permeability. Larger up-dip plume extent means more brine is encountered by the plume, and so more dissolution occurs. Since the trailing (down-dip) edge of the plume is trapped, larger up-dip extent means the plume is stretched out more, and hence CO_2 saturation is lower, leading to greater residual CO_2 trapping, less mobile CO_2, and earlier stabilization. It should be noted that while well logs from the Kimberlina region do show sand permeabilities even higher than 1000 md and even lower than 20 md, it is not known how regionally extensive such extreme features are.

3.2.3 Shale Vertical Permeability Studies

Shale vertical permeability largely controls the vertical distribution of CO_2 within the storage formation, as shown in Fig. 18. In the base case (Fig. 9), shale permeability is so low and capillary pressure strength is so high that supercritical CO_2 is effectively excluded from shale lenses. Cases SH1, SH2, SH3, and SH4 consider larger shale permeabilities, which are intended to represent sub-grid-scale heterogeneity in which sand and shale interfinger at

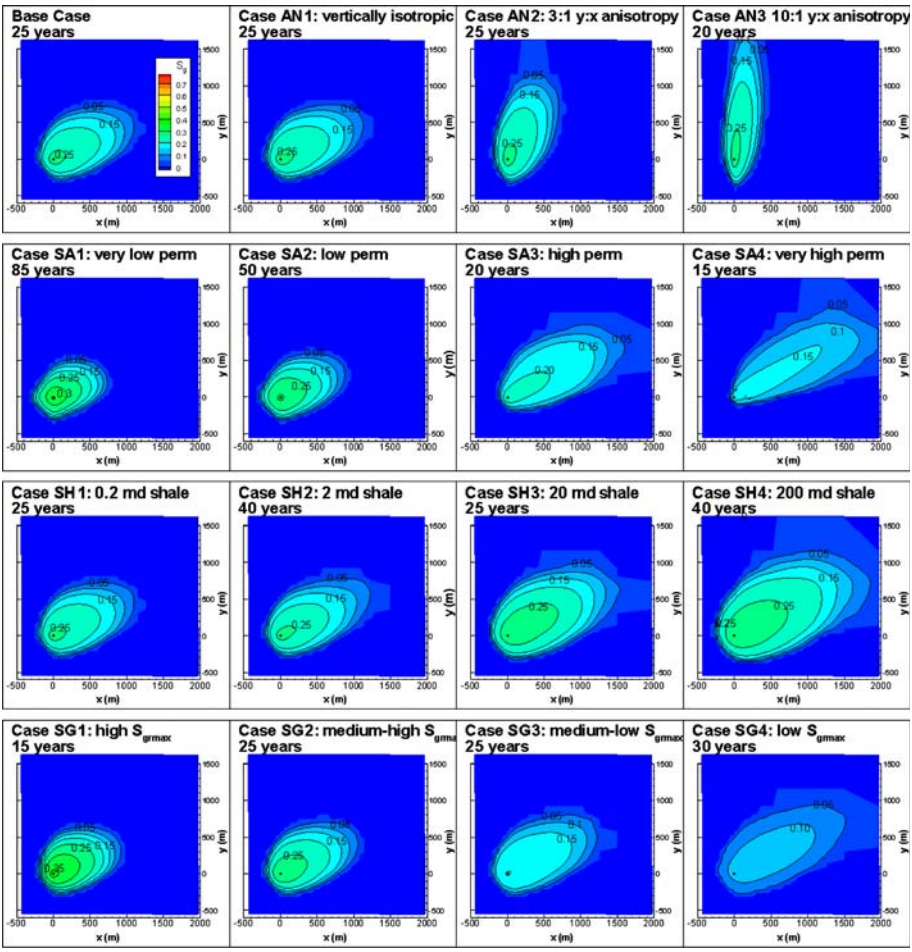

Fig. 17 Top view of stabilized supercritical CO_2 plumes for all cases, shown by plotting S_g, saturation of supercritical CO_2, in the uppermost model layer. The time to stabilization is shown for each case

scales that are less than the 55-m grid size. P_{c0} and S_{grmax} values are correlated to permeability using the same relations given for sand above. In the limiting case (Cases SH3 and SH4), shale lenses are assigned pure sand properties; therefore, shale is actually absent, and the Vedder Formation is modeled as a homogeneous sand layer. In these cases, buoyancy flow is much stronger, resulting in much greater upward migration of CO_2. This is especially true for Case SH4, in which the vertical permeability equals the horizontal permeability. For Case SH2, with shale permeability ten times smaller than that of sand permeability, supercritical CO_2 preferentially flows into sand layers, but does move into shale lenses as well. The Case SH2 plume shows more buoyancy flow than the base case, but not nearly as much as when the shale lenses are absent. For Case SH1, with a shale permeability 100 times smaller than that of sand permeability, the CO_2 distribution is indistinguishable from that of the base case, which has a shale permeability 2000 times smaller than that of sand permeability.

Increasing shale permeability has a strong effect on the plume performance measures shown in Table 4, with up-dip plume extent increasing and percent dissolved CO_2 decreas-

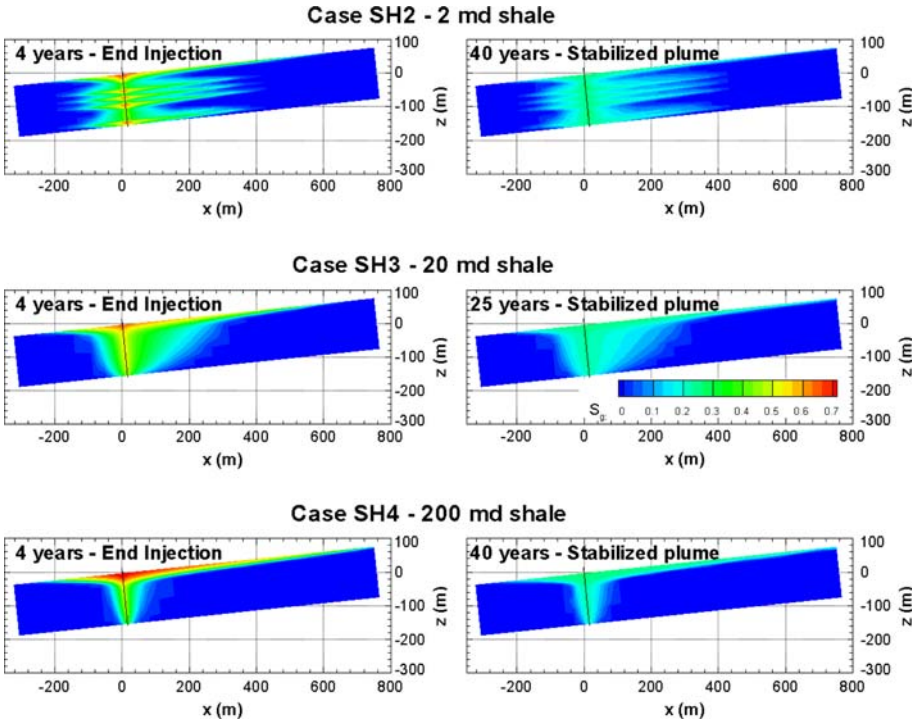

Fig. 18 East–west cross-section of the supercritical CO_2 plume at two times for sensitivity-study cases with different values of shale vertical permeability, shown by plotting S_g, saturation of supercritical CO_2, in the plane $y = 0$. Compare to base-case cross sections in Fig. 9

ing. Both these effects are a consequence of the more localized flow that occurs when the shale lenses do not divide the CO_2 into multiple plumes. CO_2 saturation in the single plume is higher than that in the five individual plumes, and so residual CO_2 trapping is diminished and up-dip migration is enhanced. Dissolution trapping also decreases, which is a consequence of the smaller CO_2/brine contact area.

Since the presence or absence of shale lenses so strongly impacts the evolution of the supercritical CO_2 plume, it is useful to examine the behavior of dissolved CO_2, in the no-shale case as well. Figure 19 shows dissolved CO_2 distributions for the Case SH4, in which the Vedder Formation is modeled as a homogeneous isotropic sand layer. As for the base case (Fig. 14), at the end of the injection period, the dissolved CO_2 distribution correlates closely with the supercritical CO_2 distribution. Thereafter, the two distributions differ significantly, as natural convection of the brine begins. Comparing Fig. 19 with Fig. 15 shows that the absence of shale lenses greatly enhances natural convection compared to the base case, which in turn enhances late-time dissolution. The integrated mass distribution in Fig. 10 illustrates how the Case-SH4 dissolved fraction, which is less than the base-case dissolved fraction when the plumes stabilize, later becomes significantly greater than it. The supercritical plume has nearly completely dissolved by 1,300 years, far sooner than the base-case dissolution time of 10,000 years.

Numerical studies of brine convection (Pruess and Zhang 2008) using much finer grid resolution than this study indicate that the details of convection (e.g., how many convection

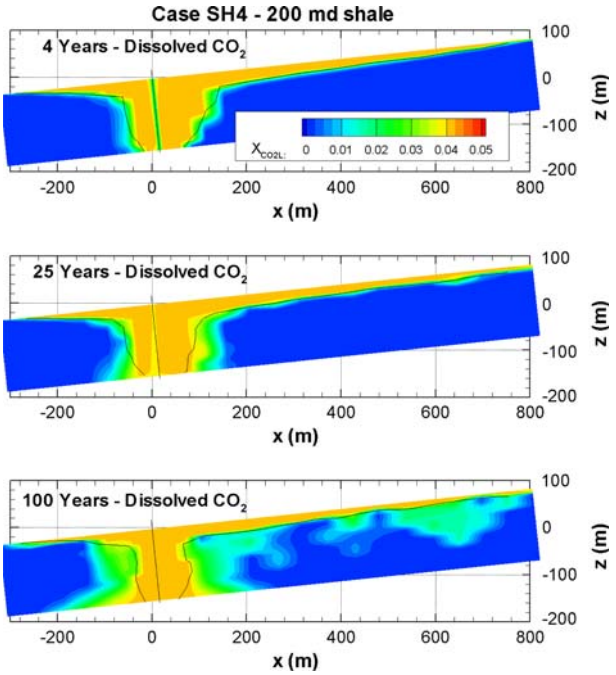

Fig. 19 East–west cross-section of the dissolved CO_2 plume at a series of times for sensitivity-study Case SH4, shown by plotting $X_{CO_{2L}}$, mass fraction of CO_2 in the aqueous phase, in the plane $y = 0$. Case SH4 models the storage formation as a homogeneous isotropic sand layer. The black contour lines show $S_g = 0$, illustrating the maximum extent of the supercritical plume

cells, individual cell locations) are quite sensitive to grid spacing, but integrated measures, such as how much CO_2 crosses a given horizontal interface, are not. Since the lateral grid resolution (55 m over most of the plume) is so coarse, the results shown in Fig. 19 should not be considered as precise predictions of dissolved CO_2 movement, but rather provide an indication of the overall magnitude of convective transport.

3.2.4 Residual Gas Saturation Studies

Unlike permeability sensitivity studies, in which a range of property values are used because of limited knowledge of subsurface property distributions, for residual gas saturation, there is even significant uncertainty in our conceptual model. To a large extent, we rely on experience with other multiphase systems, primarily from the petroleum literature, in which maximum residual gas saturation S_{grmax} is significantly above zero. The relatively few studies of CO_2/brine systems (e.g., Bachu and Bennion 2008; Benson et al. 2007; Doughty et al. 2008) support this approach, but residual CO_2 trapping is such an important process for immobilizing plumes in the absence of structural traps that further study is needed. Therefore, S_{grmax} is treated as an independent parameter, and the effect of decreasing it from the base-case value is examined (Cases SG1, SG2, SG3, and SG4). Decreasing S_{grmax} has a strong effect on the plume performance measures shown in Table 4, producing greater up-dip migration and increased time measures for plume mobility because of the diminished residual CO_2 trapping ability. In contrast, the additional up-dip migration enables more dissolution to occur.

4 Conclusions

The evolution of the CO_2 plume formed during a large-scale pilot test for geologic CO_2 storage in a moderately dipping saline aquifer has been modeled using the numerical simulator TOUGH2. Simulation results show that for the base-case, about 20% of the 1,000,000 metric tons of injected CO_2 is in dissolved form at the end of the 4-year injection period, and this percent increases to 38% by the time the CO_2 plume stabilizes at 25 years. At stabilization, of the 62% of the plume that exists as supercritical free phase, only 3% is mobile. From this time onward, plume evolution consists solely of slow dissolution, aided by natural convection of dissolved-CO_2-laden brine. The stabilized plume footprint is roughly elliptical, and is strongly asymmetric about the injection well, extending 1,300 m in the up-dip direction and 200 m in the down-dip direction. The pressure increase in response to CO_2 injection extends far beyond the plume footprint, reaching the model boundaries 8 km away from the injection well. However, the pressure response decreases rapidly with distance from the injection well, and decays rapidly in time once injection ceases.

Sensitivity studies show that uncertain model parameters permeability anisotropy, permeability itself, and maximum residual gas saturation strongly affect the direction and extent of CO_2 plume movement, demonstrating the importance of site characterization efforts to better constrain these parameters prior to CO_2 injection. Even a subtle sand lateral permeability anisotropy strongly affects plume migration direction. Sand vertical permeability anisotropy does not have much effect on plume shape when shale lenses are present, but the opposite is true for a storage formation composed solely of sand, where vertical anisotropy plays a dominant role controlling buoyancy flow of both light free-phase CO_2 and heavy dissolved-CO_2-laden brine. Even the presence of a small amount of shale, as represented by shale lenses with permeability only ten times smaller than that of sand, greatly diminishes upward buoyancy flow of free-phase CO_2.

Figure 20 summarizes the results shown in Table 4 graphically, demonstrating the trade-offs in trapping mechanisms that occur as sand permeability, shale permeability, and residual gas saturation are varied. As sand permeability increases (Fig. 20a), up-dip buoyancy flow is enhanced so up-dip plume migration increases. Dissolution trapping increases as more brine is exposed to free-phase CO_2. Residual CO_2 trapping ability decreases insofar as S_{grmax} decreases with increasing permeability, but the two time measures for plume mobility—time to 3% mobile CO_2 and time to plume stabilization—decrease significantly as sand permeability increases. This indicates that the lower CO_2 saturation resulting from greater spreading of the plume leads to more rapid residual CO_2 trapping, despite the lower S_{grmax} values.

As shale permeability increases (Fig. 20b), enhanced upward flow enables the five individual plumes to coalesce into a single plume that rises to the top of the formation, and thereafter spreads up-dip (Fig. 18). This more localized flow enables CO_2 saturation in the single plume to remain higher than in the five individual plumes, and so residual CO_2 trapping is diminished and up-dip migration is enhanced. Dissolution trapping also decreases slightly in response to the coalescence into a single plume, as the higher CO_2 saturation results in a more compact plume and thus smaller CO_2/brine contact area. The time measures for plume mobility still roughly track together, and show only a slight increase with shale permeability.

Finally, if S_{grmax} values are typically smaller than the presently-accepted ones (Fig. 20c), residual CO_2 trapping decreases, leading to greater up-dip migration, increased time measures for plume mobility, and more dissolution trapping. For small values of S_{grmax}, time to 3% mobile CO_2 becomes much longer than time to plume stabilization, because the threshold for absolute immobility (S_{grmax}) becomes much harder to reach even though the relative permeability of the plume as a whole is small enough for the plume to stabilize.

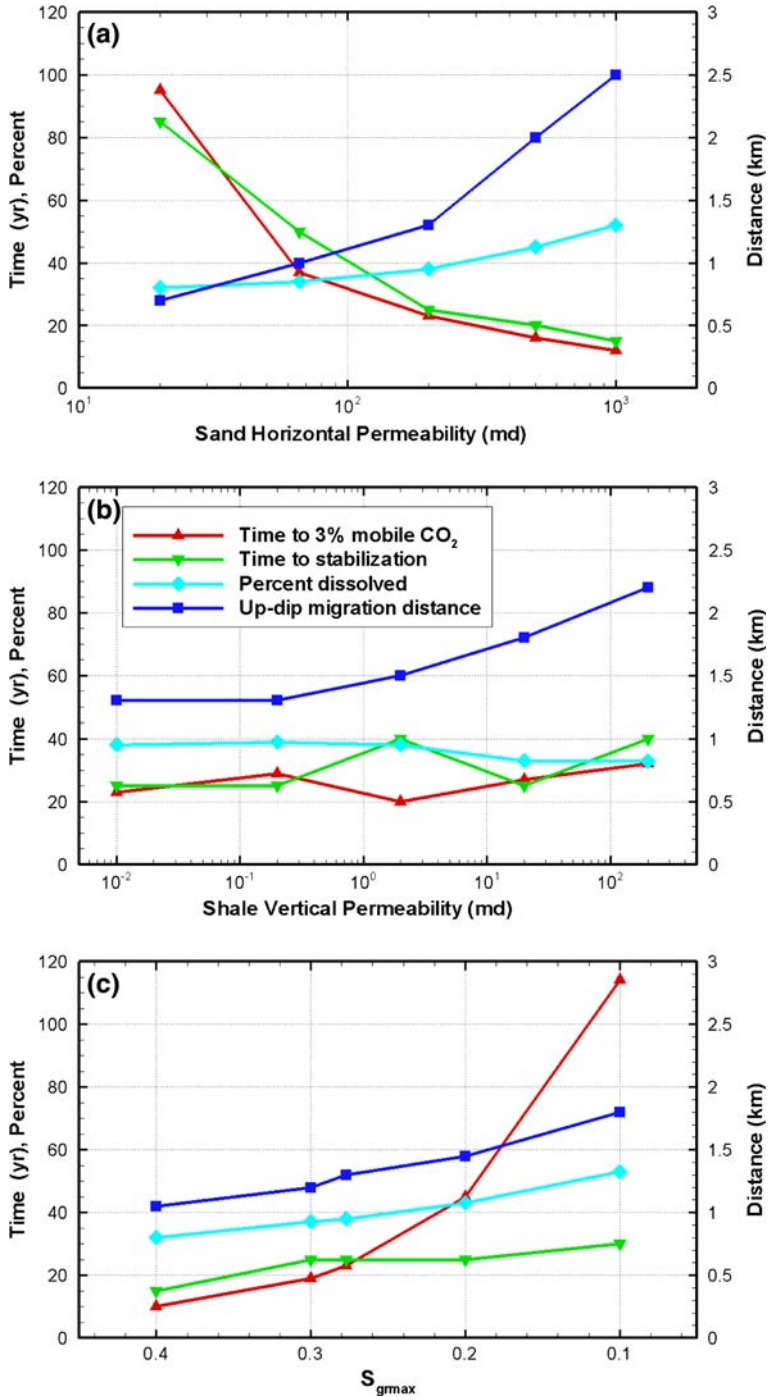

Fig. 20 Summary of the sensitivity study results for (a) sand horizontal permeability when low-permeability shale layers are present; (b) shale vertical permeability; and (c) residual gas saturation S_{grmax}

The sedimentary basin that forms California's Central Valley provides a huge potential capacity for geologic carbon storage, and the geologic stratigraphy suggests that the dipping planar structure of interleaved sands and shales that characterizes the Kimberlina model is likely very common. For the longer injection periods and much greater CO_2 volumes associated with full-scale CO_2 storage, plume migration distance will be greater and time to stabilization will be longer, but the conclusions about the interaction of trapping mechanisms drawn from this study may still be widely useful for storage locations with limited knowledge of reservoir flow parameters.

Acknowledgements Thanks are due to Jeff Wagoner of Lawrence Livermore National Laboratory for providing the geological and facies models of the Kimberlina site, to Preston Jordan for additional information on faulting, and to Larry Myer and Curt Oldenburg for insightful discussions. The careful review of this article by Kenzi Karasaki and two anonymous reviewers is appreciated. This study was supported in part by WESTCARB through the Assistant Secretary for Fossil Energy, Office of Sequestration, Hydrogen, and Clean Coal Fuels, National Energy Technology Laboratory (NETL), and by Lawrence Berkeley National Laboratory under U.S. Department of Energy Contract No. DE-AC02-05CH11231.

References

Bachu, S., Bennion, D.B.: Effects of in-situ conditions on relative permeability characteristics of CO_2-brine systems. Environ. Geol. **54**(8), 1707–1722 (2008)

Bachu, S., Gunter, W.D., Perkins, E.H.: Aquifer disposal of CO_2: hydrodynamic and mineral trapping. Energy Convers. Manage. **35**(4), 269–279 (1994)

Benson, S.M., Miljkovic, L., Tomutsa, L., Doughty, C.: Relative permeability and capillary pressure controls on CO_2 migration and brine displacement—elucidating fundamental mechanisms by laboratory experiments and simulation. Sixth National Conference on Carbon Capture and Sequestration, National Energy Technology Lab, Pittsburgh PA (2007)

Doughty, C.: Modeling geologic storage of carbon dioxide: comparison of non-hysteretic and hysteretic characteristic curves. Energy Convers. Manag. **48**(6), 1768–1781 (2007)

Doughty, C., Myer, L.R.: Scoping calculations on leakage of CO_2 in geologic storage: The impact of overburden permeability, phase trapping, and dissolution. In: McPherson, B., Sundquist, E. (eds.) Science and Technology of Carbon Sequestration, American Geophysical Union, Washington DC (2009, in press)

Doughty, C., Freifeld, B.M., Trautz, R.C.: Site characterization for CO_2 geologic storage and vice versa—the Frio brine pilot Texas USA as a case study. Environ. Geol. **54**(8), 1635–1656 (2008)

Ennis-King, J., Paterson, L.: Role of convective mixing in the long-term storage of carbon dioxide in deep saline formations (SPE 84344). Soc. Petrol. Eng. J. **10**(3), 349–356 (2005)

Gherardi, F., Xu, T., Pruess, K.: Numerical modeling of self-limiting and self-enhancing caprock alteration induced by CO_2 storage in a depleted gas reservoir. Chem. Geol. **244**(1-2), 103–129 (2007)

Holtz, M.H.: Residual gas saturation to aquifer influx: a calculation method for 3-D computer reservoir model construction (SPE 75502). SPE gas technology symposium, Calgary, Alberta (2002)

Jordan, P., Doughty, C: Sensitivity of CO_2 migration estimation on reservoir temperature and pressure uncertainty. GHGT-9 Conference, Washington DC (2008)

Land, C.S.: Calculation of imbibition relative permeability for two- and three-phase flow from rock properties (SPE 1942). Soc. Petrol. Eng. J. **8**, 149–156 (1968)

Pruess, K., Spycher, N.: ECO2N—A fluid property module for the TOUGH2 code for studies of CO_2 storage in saline aquifers. Energy Convers. Manage. **48**(6), 1761–1767 (2007)

Pruess, K., Zhang, K.: Numerical modeling studies of the dissolution-diffusion-convection process during CO_2 storage in saline aquifers. Rep. LBNL-1243E. Lawrence Berkeley National Laboratory, Berkeley CA (2008)

Pruess, K, Oldenburg, C.M., Moridis, G.J.: TOUGH2 User's Guide, Version 2.0. Rep. LBNL-43134. Lawrence Berkeley National Laboratory, Berkeley CA (1999)

Pruess, K., Xu, T., Apps, J., García, J.: Numerical modeling of aquifer disposal of CO_2 (SPE 83695). Soc. Petrol. Eng. J. **8**(1), 49–60 (2003)

Spycher, N., Pruess, K.: CO_2-H_2O mixtures in the geological sequestration of CO_2: II Partitioning in chloride brines at 12 − 100°C and up to 600 bars. Geochim. Cosmochim. Ac. **69**(13), 3309–3320 (2005)

van Genuchten, M. Th.: A closed-form equation for predicting the hydraulic conductivity of unsaturated soils. Soil Sci. Soc. Am. J. **44** (5):892-898 (1980)

Wagoner, J.: 3D Geologic modeling of the southern San Joaquin basin for the Westcarb Kimberlina demonstration project—a status report. Rep LLNL-TR-410813. Lawrence Livermore National Laboratory, Livermore CA (2009)

Xu, T., Apps J., Pruess, K.: Reactive geochemical transport simulation to study mineral trapping for CO_2 disposal in deep Arenaceous formations. J. Geophys. Res. **108** (B2): 2071 (2003). doi:10.1029/2002JB001979

Xu, T., Apps, J., Pruess, K.: Mineral sequestration of carbon dioxide in a sandstone-shale system. Chem. Geol. **217**, 295–318 (2005)

Xu, T., Sonnenthal, E.L., Spycher, N., Pruess, K.: TOUGHREACT - A simulation program for non-isothermal multiphase reactive geochemical transport in variably saturated geologic media: applications to geothermal injectivity and CO_2 geological sequestration. Comput. Geosci. **32**, 145–165 (2006)